Geomechanics and Engineering, *Vol. 37, No. 5 (2024) 467-474*
https://doi.org/10.12989/gae.2024.37.5.467

Application of Ground Penetrating Radar (GPR) coupled with Convolutional Neural Network (CNN) for characterizing underground conditions

Dae-Hong Min[a] and Hyung-Koo Yoon*

Department of Construction and Disaster Prevention Engineering, Daejeon University, Daejeon 34520, Republic of Korea

(*Received March 12, 2024, Revised May 7, 2024, Accepted May 8, 2024*)

Abstract. Monitoring and managing the condition of underground utilities is crucial for ground stability. This study aims to determine whether images obtained using ground penetrating radar (GPR) accurately reflect the characteristics of buried pipelines through image analysis. The investigation focuses on pipelines made from different materials, namely concrete and steel, with concrete pipes tested under various diameters to assess detectability under differing conditions. A total of 400 images are acquired at locations with pipelines, and for comparison, an additional 100 data points are collected from areas without pipelines. The study employs GPR at frequencies of 200 MHz and 600 MHz, and image analysis is performed using machine learning-based convolutional neural network (CNN) techniques. The analysis results demonstrate high classification reliability based on the training data, especially in distinguishing between pipes of the same material but of different diameters. The findings suggest that the integration of GPR and CNN algorithms can offer satisfactory performance in exploring the ground's interior characteristics.

Keywords: convolutional neural network; ground penetrating radar; image analysis; stability

1. Introduction

Urban maintenance encompasses the crucial task of safely managing underground utilities, which include infrastructure such as telecommunications, water supply, and sewage systems (Guzman and Payano 2023; Jiao *et al.* 2024; Xu *et al*. 2024, Zhou *et al*. 2024). In South Korea, newly planned cities have adopted the construction of utility tunnels to collectively house underground utilities within a designated space, aiming for their safe management. However, utilities installed before this practice are not managed in a unified manner like those in utility tunnels; instead, they are individually managed based on the characteristics at the time of construction (Oner *et al.* 2023).

In areas where design drawings are well-managed and preserved, it is possible to infer the location of underground utilities and establish plans for maintenance and renewal. However, in regions developed long ago, where managing design drawings is challenging, locating the utilities can be difficult. Therefore, identifying the location of underground utility pipes is essential to address these issues, and non-destructive exploration methods are commonly employed for this purpose. The most widely used non-destructive test methods for locating underground utilities include seismic exploration, electrical resistivity exploration, and ground penetrating radar (GPR) exploration (Hong *et al*. 2022, Min and Yoon 2023, Olabode and San 2023). Seismic and electrical resistivity explorations can provide detailed observations of the location and condition of deeply buried utilities but require the separate installation of geophones and electrodes on the ground surface, which can be challenging (Iftikhar *et al.* 2023). If the surface is a paved road, removing the pavement layer to transmit energy into the underground poses a problem, limiting its application in urban areas. However, GPR, which uses electromagnetic waves, allows for the inference of the underground condition without the need for separate sensor installation on the ground surface, making it widely used for assessing the internal state of urban areas.

Fąfara *et al*. (2018) utilized Ground Penetration Radar (GPR) techniques to observe the extent of oil leakage from pipelines buried underground. They assessed the presence of leaks by observing changes in permittivity, which cause attenuation of electromagnetic waves, when oil leaks into the ground from damaged pipelines. Crocco *et al.* (2010) presented an interpretation method for waveforms acquired through GPR equipment, modeling a method that performs inverse tomography by imaging reflection times. The method used was the finite difference time-domain (FDTD), proposing a technique to detect leakage phenomena around pipelines through forward modeling around the buried pipes. Additionally, Araneo *et al*. (2005) conducted GPR experiments to quantitatively assess the extent of damage by artificially damaging pipelines and measuring the reflected voltage values. The damage was categorized into depths of 1 mm, 2 mm, and complete damage, presenting a method to distinguish each condition through the time difference in the GPR's reflected voltage. As seen in previous studies, GPR is being applied to develop various experimental conditions and interpretation methods for assessing the condition of pipelines buried underground. However, there are limitations in inspecting conditions such as cracks if there is no information about the buried utilities.

*Corresponding author, Associate Professor
E-mail: hyungkoo@dju.ac.kr
[a]Ph.D. Candidate

ISSN: 2005-307X (Print), 2092-6219 (Online)

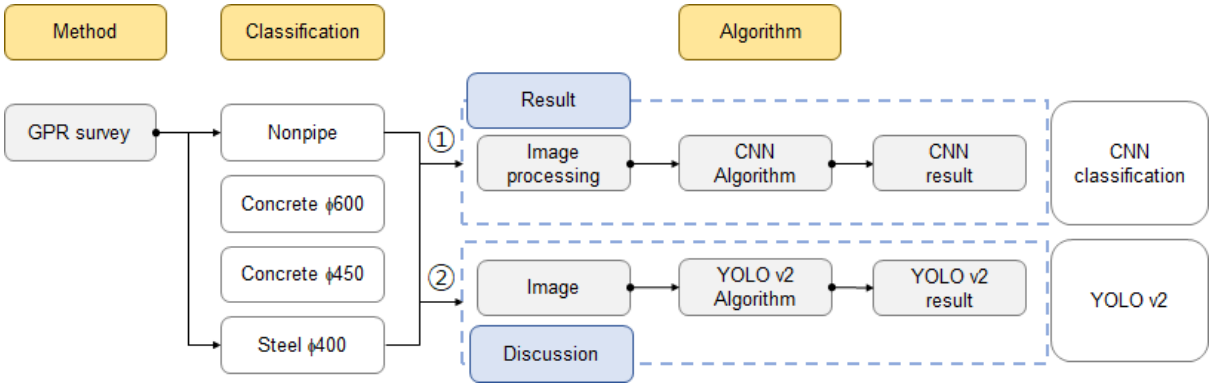

Fig. 1 Flow chart of this study. The symbol of ϕ denotes the diameter of buried pipe

This is because the reflected waveforms of GPR change depending on the material state of the buried object, requiring prior knowledge of the material characteristics of the buried object for subsequent analysis. Therefore, without information on the buried utilities, it is necessary to know the materials and diameters of the utilities to understand the purpose of the pipelines and discuss potential issues later. The paper aimed to present a method to identify the type and diameter of pipelines through GPR exploration, assuming no prior information about the underground utilities. For this purpose, machine learning techniques, which are widely used recently, were applied, and the convolutional neural network (CNN) interpretation technique was implemented to classify images acquired through GPR exploration as shown in Figure 1. Figure 1 represents a flowchart applying CNN classification(① algorithm) and object detection YOLO(② algorithm) methods based on the same input data.

The paper starts with an introduction to the fundamental concepts of Ground Penetration Radar (GPR) and the theoretical background of convolutional neural networks (CNN) as an analytical tool. It also offers a comprehensive simulation of the target site. The field experiment section details the materials and diameters of the buried pipes, along with the number of images obtained through GPR exploration and their quantitative evaluation. In the results section, the paper simulates the reflected waveforms observed in the GPR exploration images and ultimately validates the classification reliability after implementing the CNN technique.

2. Background theory

2.1 Ground-penetrating radar (GPR)

Ground-penetrating radar (GPR) is a non-destructive investigation method that allows for the inference of ground conditions without the need for drilling or sensor installation. It functions by injecting energy into the ground in the form of pulses using electromagnetic waves within the high-frequency range (10MHz to 2.6 GHz) and capturing the waveforms that are reflected from surface and internal discontinuities. The transmitter and receiver are connected as a unit and are mounted on a wheeled frame, facilitating easy movement and enabling immediate measurement of the internal ground condition. Permittivity is the characteristic that describes how the flow of current changes when an electric field is applied, and the internal condition is evaluated by considering the extent to which the reflected waveforms are attenuated due to differences in permittivity. While GPR offers the advantage of assessing ground conditions without the need for drilling, its penetration depth can be limited if there are materials within the ground that interfere with the flow of current, leading to concentrated energy of the emitted electromagnetic waves. This limitation is referred to as the exploration depth and is closely associated with the electrical conductivity of the medium. Consequently, the central frequency of GPR is selected based on the user's objectives and the internal condition of the ground. In this study, two frequencies, 200 MHz and 600 MHz, were employed to investigate the condition of pipelines

2.2 Convolution Neural Network(CNN)

The Convolutional Neural Network (CNN) algorithm is a method based on machine learning for analyzing images (Benemaran and Esmaeili-Falak 2023, Fereidooni and Karimi 2023, Kim and Yoon 2023). It shares similarities with artificial neural networks, possessing input and output layers, with hidden layers in between to connect them (Samadi *et al*. 2023). However, distinct from artificial neural networks, CNNs incorporate convolution and pooling layers to extract image patterns. The convolution process applies filter values to each pixel of the quantified image, producing a feature map that emphasizes key features. These filters are built using kernel functions, which typically consist of unit matrix and vector values. Furthermore, the pooling layer simplifies the output of the original image by reducing the number of parameters required for training, thus enhancing the speed of training. Leveraging these principles, the CNN algorithm identifies patterns in images and delivers classification results tailored to the user's goals.

3. Test area

The objective of this study is to assess whether GPR images, captured in areas with buried utilities of different

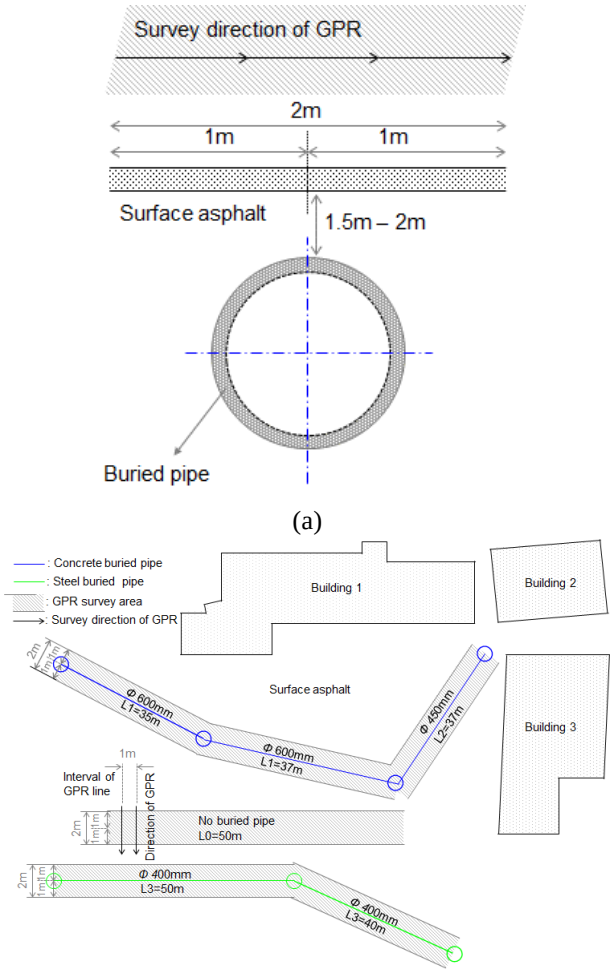

Fig. 2 Test site of ground penetrating radar (GPR) experiments: (a) direction of GPR investigation and (b) positions of buried pile and GPR profiles

materials and diameters, can be accurately classified by their characteristics after the application of the CNN technique. Experiments were carried out in a parking lot in Daejeon, South Korea, featuring pipelines of various materials and diameters, with Fig. 2 providing a top view. Additionally, this figure categorizes the materials of the buried pipelines as concrete and steel, identifying L-1 and L-2 as cylindrical concrete pipes as per the design drawings. The diameters of pipelines L-1 and L-2 are 400 mm and 600mm, respectively, and the diameter of the steel pipe, L-3, is 400 mm. In the design drawings, the burial depths of the conduits are shown as 1.5 - 2 m. The GPR exploration aimed for a penetration depth of approximately 2 m, taking into account the diameters of the pipelines and the depth of the surface, with frequency bands set at 200 MHz and 600 MHz. The equipment was configured to utilize dual frequencies, with the goal of examining the characteristics of images obtained at both frequencies. Image data were gathered from three points surrounding each pipeline: one in the orthogonal direction and two in diagonal directions, conducting GPR scans at 1m intervals. The numbers of images obtained at the locations of L-1, L-2, and L-3 were 100, 150, and 150, respectively, amassing a total of 400 cross-sectional images. Furthermore, to validate the reliability of the CNN learning and classification process, GPR exploration was performed at locations without buried utilities within the same experimental area, resulting in an additional 100 images.

4. Result

4.1 GPR images

The GPR result images are presented in Fig. 3, categorized by the type of buried pipe. The classifications include areas without buried pipes, concrete buried pipes (600mm diameter), concrete buried pipes (diameter), and steel buried pipes (400 mm diameter), each labeled for CNN classification. Fig. 3(a) displays the representative GPR images for areas lacking buried pipes, highlighting the ends and the midpoint of the area, where layer differentiation is evident through reflected waves. The surface is covered with asphalt, and a pronounced reflective waveform is detected at a depth of 0 m. The section from the surface down to a depth of 0.5 m is presumed to be the upper stratum, likely a sand layer. Beyond a depth of 1.1 m, it is believed to be the original ground stratum, characterized by repeated strong reflective waveforms, suggesting multiple layers due to compaction efforts. Fig. 3(b) illustrates the reflective wave image for a concrete buried pipe (450 mm diameter), with a hyperbola visible around a depth of 2 m. This likely aligns with the installation depth of the buried pipe as specified in the parking lot design plans. Fig. 3(c) depicts the reflective wave image for a concrete buried pipe (600 mm diameter), situated at a similar depth of around 2 m as seen in Fig. 3(b). The maximum size of the hyperbola is roughly 1.5 m for Fig. 3(b) and about 1.8 m for Fig. 3(c). This size discrepancy is attributed to the pipe diameter, with the 600mm diameter reflecting a larger radius than the 450 mm. Fig. 3(d) features the steel buried pipe, which, akin to the concrete buried pipes, exhibits a hyperbola at a depth of about 2 m, but with a reflection radius of approximately 1m, smaller than those observed in Figs. 3(b) and 3(c). This variation is understood to stem from the differences in pipe diameters, leading to distinct sizes of reflected waveforms as previously explained.

4.2 Preprocessing

CNN interpret images as vector numerical values and RGB colors. To enhance classification accuracy with CNN algorithms, preprocessing was conducted on GPR reflection images in two steps. The initial step involved isolating only the hyperbolic sections from the GPR reflection cross-sectional images to accurately differentiate vector values, subsequently classifying them by label. This research identified the hyperbolic shape of electromagnetic waves, indicative of buried pipes, as essential for determining the location, type, and size of these pipes. Thus, to precisely detect hyperbolas across the entire image, hyperbola extraction was performed for each label. Figs. 4(a) presents an image from an area devoid of buried pipes, where the

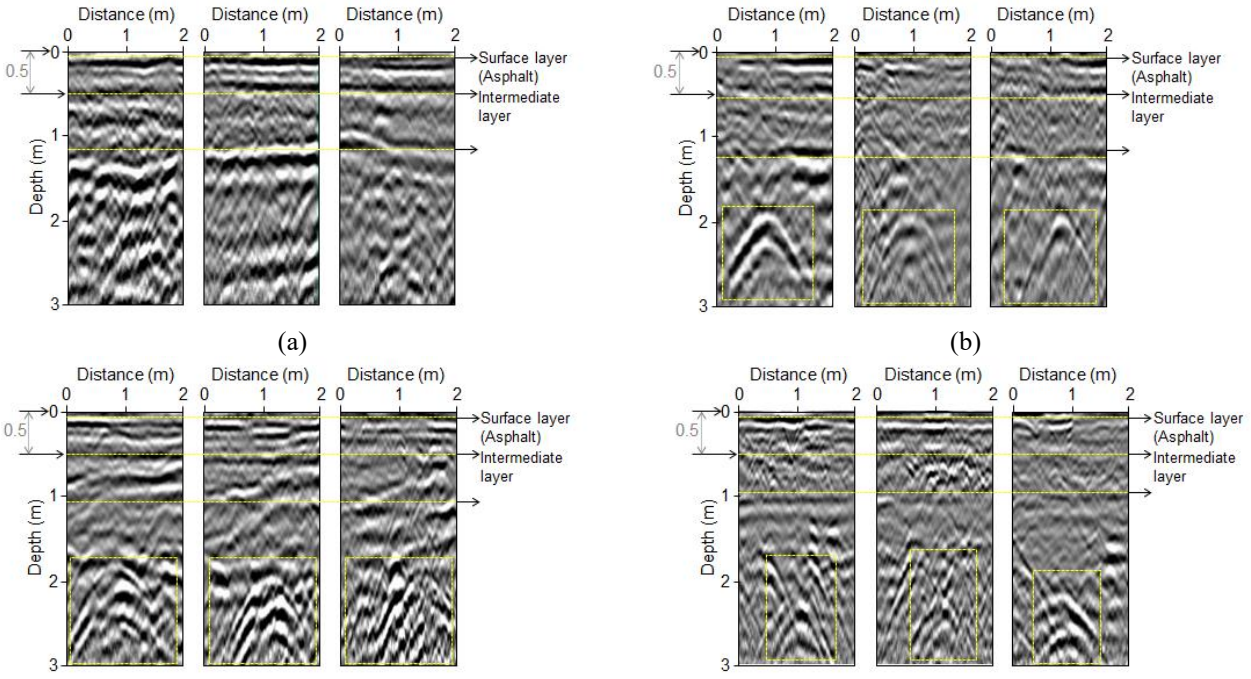

Fig. 3 Extracted images of ground penetrating radar (GPR) experiments: (a) area without buried pipe, (b) concrete buried pipe (600 mm diameter), (c) concrete buried pipe (450 mm diameter) and (d) steel buried pipes (400 mm diameter)

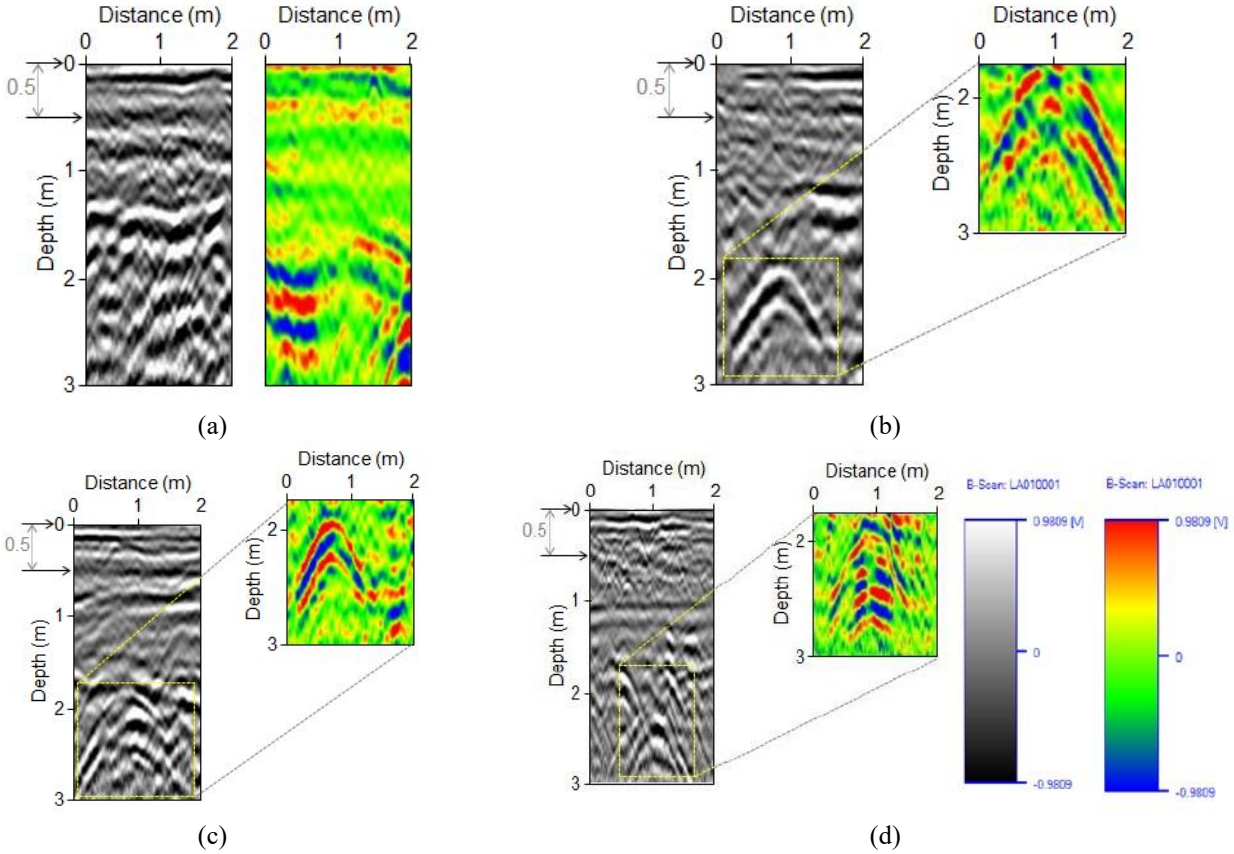

Fig. 4 Preprocessing of extracted images for applying convolution neural network (CNN): (a) area without buried pipe, (b) concrete buried pipe (600 mm diameter), (c) concrete buried pipe (450 mm diameter) and (d) steel buried pipes (400 mm diameter)

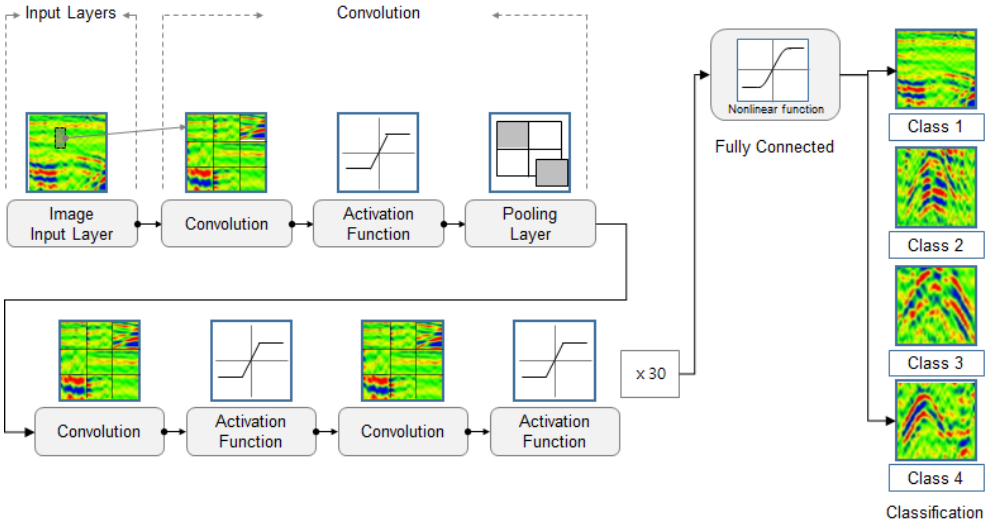

Fig. 5 Architecture of Res-Net 101 algorithm for performing classification

Table 1 Hyperparameter settings at each layer

	Convolution	Pooling	Optimization
Filter size	560, 420	-	-
Stride	2, 2	-	-
Padding	0, 0, 0, 0	-	-
Pool size	-	5	-
Solver	-	-	Adam
Initial learning rate	-	-	0.001

entire stratum image is utilized for training due to the absence of hyperbolas. Fig. 4(b) illustrates the extraction of a hyperbola from a concrete buried pipe (600 mm diameter) image, with a yellow box marking the rectangular boundary of the extracted hyperbola. Fig. 4(c) shows the hyperbolic section extracted with a yellow boundary for a concrete buried pipe (450 mm diameter); the boundary size appears relatively larger due to the smaller diameter of the pipe compared to that in Fig. 4(b). Fig. 4(d) displays the image with the hyperbolic shape extracted from an iron pipe. The second approach sought to improve image recognition and accuracy by modifying RGB values, applying a color inversion effect to the original grayscale imagery with red, blue, yellow, and green in Fig. 4. This inversion effect was applied to all labels in Figs. 4(a)-4(d), making the hyperbolic sections and areas with strong reflective amplitudes more visually distinguishable. The black and white and colorful inversion effects vary in reflection intensity (volt) according to each color and its intensity, and their range is shown in Fig. 4(d). The intensity range for all conduits is the same, ranging from a minimum of -0.9809 volts to a maximum of 0.9809 volts.

4.3 Convolution neural network

To perform classification with CNN algorithms, a suitable dataset is essential. The input labels consist of areas without buried pipes, concrete buried pipes (600 mm diameter), concrete buried pipes (450 mm diameter), and steel pipes (400 mm diameter), as depicted in Fig. 3. The output labels are assigned as classes 1, 2, 3, and 4, corresponding to the order of the input data. The dataset comprises a total of 254 images: 52 for areas without buried pipes, 72 for concrete buried pipes (600 mm diameter), 38 for concrete buried pipes (450 mm diameter), and 92 for steel pipes (400 mm diameter).

The variance in the number of images per label can introduce bias into the training data, potentially skewing prediction accuracy in favor of labels with more images. To address this, the dataset was augmented to equalize the number of images for each label to 110, using data augmentation techniques. These techniques include random rotation of the original images, random pixel shifting, and random scaling. Random rotations were applied within a range of 0° to 180°, and pixel shifts for both vertical and horizontal translations were adjusted to a range from 0 to 1. Random scaling was avoided to prevent distortion of the original data, and the chosen methods aimed to minimize alterations to the original data. Data validation was conducted using the k-fold method, with the training and testing data split into a 7:3 ratios. This split was not sequential but randomly selected to mitigate prediction bias. Ultimately, out of the augmented dataset of 440 images, 70% (308 images) were allocated for training and 30% (132

(a)

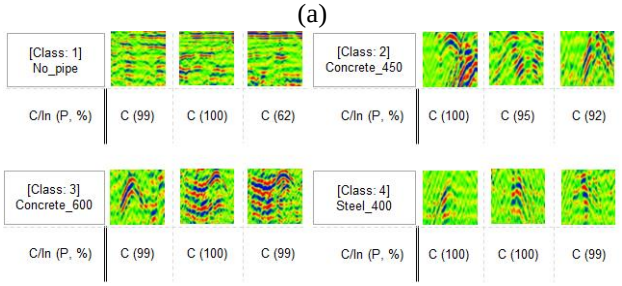

(b)

Fig. 6 Result of Res-Net 101 algorithm: (a) distributions of accuracy with iteration and (b) accuracies according to classes 1-4

images) for testing to operationalize the CNN.

Transfer learning leverages a pre-trained neural network with proven accuracy, enabling predictions on new data with only minor adjustments to hyperparameters and achieving high accuracy with relatively small data volumes. The ResNet-101 algorithm employed in this study features an architecture as depicted in Fig. 5. The input layer is composed of 440 images categorized into 4 labels and includes a convolution layer tasked with image recognition. This layer utilizes the kernel function to recognize the vector values of image data. Additionally, it incorporates an activation function and a pooling module, which are essential for formulating a mathematical model for image data classification and for reconfiguring pixel capacity to facilitate efficient learning. Structurally, the ResNet-101 architecture consists of modules where convolution and activation functions are combined, systematically normalizing data across a total of 30 layers in repetition. Ultimately, classification for each label is executed through a fully connected layer that amalgamates all weights and biases. Hyperparameters affect the output of results based on training, and the values set in this study are as shown in Table 1. Hyperparameter fine-tuning was applied to the convolution, activation function, and pooling module, with adjustments made to stride (2, 2), ReLU function, and pool size (5), respectively. Moreover, the optimization algorithm minimizes the error rate via backpropagation, updating weights and biases, employing Adam as the solver and setting an initial learning rate of 0.0001.

The finely adjusted ResNet-101 conducted classification predictions on 440 data points, displaying the prediction outcomes as shown in Fig. 6(a). Fig. 6(a) displays the accuracy and error metrics for both training and testing phases across different epochs. The minibatch size, established at 5, facilitates data clustering for more effective learning, with each cluster of five data points undergoing a single iteration of learning. An epoch encompasses 100 learning iterations, with validation occurring once every 100 iterations. Upon completing the training, the final validation outcomes demonstrated an accuracy of 92.11% and an error rate of 0.32, affirming the algorithm's efficacy following fine-tuning. This algorithmic framework was employed to input three samples per label as new data to calculate prediction probabilities. The results of these prediction probabilities are illustrated in Fig. 6(b), where C/In and P denote correct/incorrect classifications and prediction, respectively. A sample is labeled as “C” if it is correctly classified under its respective label, and as “In” if it is misclassified under a different label. Furthermore, the prediction probability indicates the chance of a sample being classified into one of the four labels. Class 1, indicative of areas without buried pipes, revealed prediction probabilities of 99% and 100% for two samples, whereas one sample exhibited a 62% probability, presumably due to a lower intensity of color inversion. Classes 2, 3, and 4, corresponding to concrete buried pipes of 600mm and 400mm, and steel buried pipes of 400mm, respectively, showed high average prediction probabilities of 95.7%, 99.3%, and 99.7%

5. Discussion

In this study, the YOLO v2 algorithm, commonly utilized for object recognition, was further applied to assess and compare the accuracy of hyperbola recognition. The images employed were unprocessed originals, classified under the same labels as those used for ResNet-101, to obtain the recognition outcomes. The recognition results from YOLO v2 are depicted in Fig. 7(a), with the degree of recognition delineated by yellow rectangular boundaries. The upper section of Fig. 7(a) demonstrates precise detection of hyperbolas according to their respective labels, with the hyperbolas' locations being accurately identified. Concrete buried pipes of 600 mm, 450 mm, and 400 mm were distinguished and detected; however, the detection of the hyperbolas' sizes, which fell outside the box boundaries, indicates a deficiency in size detection capability. The lower section of Fig. 7(a) illustrates instances of failed hyperbola detection, categorized into three primary scenarios: the first involves detecting hyperbolas at dual locations or with overlapping labels, the second pertains to the inability to detect the hyperbola itself, and the third involves detecting non-hyperbola positions. These scenarios were deemed to have an accuracy of 0%, while accurate detection of a hyperbola's position in accordance with its label was considered to achieve 100% accuracy. YOLO v2 detection was conducted on 440 items, and the average accuracy across these items was determined.

Fig. 7(b) displays the average accuracy graph for ResNet-101 and YOLO v2, with comparisons conducted across each label. Across all labels, ResNet-101 achieved higher average accuracies, with differences ranging from a minimum of 48.0% to a maximum of 87.6%. Apart from an accuracy of 84.0% for regions without buried pipes, ResNet-101 showed accuracies above 95% for all labels, in

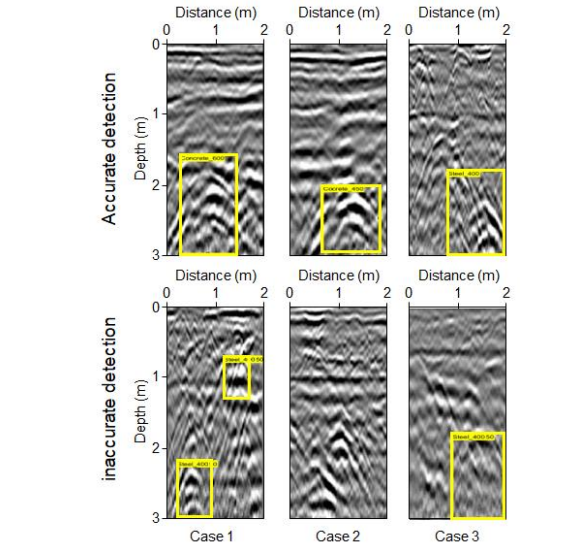

(a)

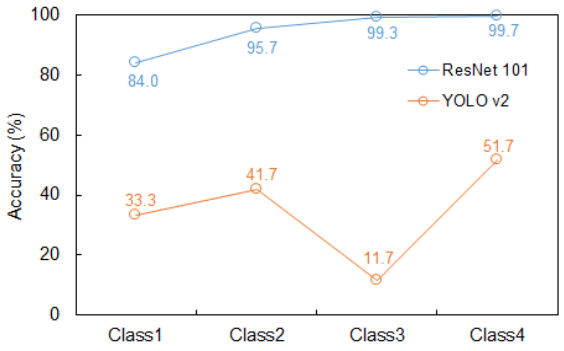

(b)

Fig. 7 Comparison of accuracies based on YOLO v2 and ResNet-101 algorithms: (a) detected hyperbola through YOLO v2 algorithm and (b) distributions of averaged accuracies

contrast to YOLO v2, which recorded accuracies below 50%. The reason why the accuracy of ResNet 101 is higher than that of the YOLO algorithm appears to be due to the preprocessing of hyperbola and RGB values to clarify image recognition. Additionally, RGB values have unique values depending on the color compared to black and white, making them effective for image recognition. This accuracy comparison underscores the significance of data preprocessing, suggesting that preprocessing approaches undertaken are appropriate for GPR image classification and prediction.

6. Conclusions

This study sought to predict the characteristics of underground pipes by integrating ground penetrating radar (GPR) with a convolutional neural network (CNN), with the detailed conclusions as follows:

- GPR exploration was carried out according to the material and diameter of the buried utilities, resulting in the acquisition of a total of 400 images. Furthermore, an additional 100 images were collected from areas lacking buried utilities to validate the reliability.
- Classification was carried out using the CNN technique, with ResNet-101 being the algorithm employed. The classification outcomes revealed an accuracy exceeding 99% across all four classes, indicating that these results can be used to deduce the condition of the buried pipes.
- The reliability of the outcomes was further validated through the application of the YOLO v2 algorithm, widely utilized for object recognition. The YOLO v2 algorithm demonstrated a reliability below 50%, suggesting that the approach introduced in this research is comparatively superior. Consequently, it is anticipated that linking the CNN algorithm with a preprocessing step would yield more dependable results

Acknowledgments

This research was supported by the Basic Science Research Program through the National Research Foundation of Korea (NRF) funded by the Ministry of Education (NRF-2020R1A2C2012113).

References

Araneo, R., Celozzi, S., Maradei, F. and Potini, G. (2005), "Fault detection in conductive pipelines by time domain reflectometry", *WSEAS Transactions on Systems*, **4**(12), 2317-2321. https://doi.org/10.1109/AFRICON.2004.1406701.

Benemaran, R.S. and Esmaeili-Falak, M. (2023), "Predicting the Young's modulus of frozen sand using machine learning approaches: State-of-the-art review", *Geomech. Eng.*, **34**(5), 507-527. https://doi.org/10.12989/gae.2023.34.5.507.

Crocco, L., Soldovieri, F., Millington, T. and Cassidy, N.J. (2010), "Bistatic tomographic GPR imaging for incipient pipeline leakage evaluation", *Progress In Electromagnetics Research*, **101**, 307-321. https://doi.org/10.2528/PIER09122206.

Fąfara, Z., Lewandowska-Śmierzchalska, J. and Matuła, R. (2018), "Oil pipeline leak detection using GPR method-simple case study", *AGH Drilling, Oil, Gas*, **35**(1), 165-171. https://doi.org/10.7494/drill.2018.35.1.165.

Fereidooni, D. and Karimi, Z. (2023), "Predicting rock brittleness indices from simple laboratory test results using some machine learning methods", *Geomech. Eng.*, **34**(6), 697-726. https://doi.org/10.12989/gae.2023.34.6.697.

Guzman, I.L. and Payano Jr, C. (2023), "Use of repurposed whole textile for enhancement of pavement soils", *Int. J. Geo-Eng.*, **14**(1), 12. https://doi.org/10.1186/s40703-023-00190-1.

Hong, W.T., Lee, J.S., Lee, D. and Yoon, H.K. (2022), "Estimation of bulk electrical conductivity in saline medium with contaminated lead solution through TDR coupled with machine learning", *Process Saf. Environ. Protect.*, **161**, 58-66. https://doi.org/10.1016/j.psep.2022.03.018.

Iftikhar, C.M.A., Khan, A.S. and Nambori, V. (2023), "The effect of temperature on the mechanical behavior of Berea sandstone under confining pressure: experiments", *Int. J. Geo-Eng.*, **14**(1), 18. https://doi.org/10.1186/s40703-023-00191-0.

Jiao, N., Wan, X., Ding, J., Zhang, S. and Liu, J. (2024), "Pipeline deformation caused by double curved shield tunnel in soil-rock composite stratum", *Geomech. Eng.*, **36**(2), 131-143. https://doi.org/10.12989/gae.2024.36.2.131.

Kim, S. and Yoon, H.K. (2023), "Application of classification coupled with PCA and SMOTE, for obtaining safety factor of landslide based on HRA", *Bull. Eng. Geol. Environ*., **82**(10), 381. https://doi.org/10.1007/s10064-023-03403-0.

Min, D.H., Jang, B.S. and Yoon, H.K. (2023), "Application of infrared thermography for estimating residual stress in ground anchors for maintenance", *Scientific Reports*, **13**(1), 36. https://doi.org/10.1038/s41598-022-27222-7.

Olabode, O.P. and San, L.H. (2023), "Analysis of soil electrical resistivity and hydraulic conductivity relationship for characterisation of lithology inducing slope instability in residual soil", *Int. J. Geo-Eng*., **14**(1), 7. https://doi.org/10.1186/s40703-023-00184-z.

Oner, C., Bildik, S. and Frost, J.D. (2023), "Numerical investigation of effect of geotextile and pipe stiffness on buried pipe behavior", *Geomech. Eng*., **34**(6), 611-621. https://doi.org/10.12989/gae.2023.34.6.611.

Samadi, H., Hassanpour, J. and Rostami, J. (2023), "Prediction of earth pressure balance for EPB-TBM using machine learning algorithms", *Int. J. Geo-Eng*., **14**(1), 21. https://doi.org/10.1186/s40703-023-00198-7.

Xu, M.Z., Cui, Z.D. and Yuan, L. (2024), "Effect of relative stiffness on seismic response of subway station buried in layered soft soil foundation", *Geomech. Eng*., **36**(2), 167-181. https://doi.org/10.12989/gae.2024.36.2.167.

Zhou, J., Ding, Z., Huang, J., Yang, X. and Ma, M. (2024), "The tunnel model tests of material development in different surrounding rock grades and the force laws in whole excavation-support processes", *Geomech. Eng*., **36**(1), 51-69. https://doi.org/10.12989/gae.2024.36.1.051

IC